

# Numerical study of the effect of the noseleaf on biosonar beamforming in a horseshoe bat

Qiao Zhuang and Rolf Müller

*School of Physics and Microelectronics, Shandong University, Hongjia Lou 5, 250100 Jinan, China*

(Received 18 April 2007; revised manuscript received 22 August 2007; published 5 November 2007)

Around 300 bat species are known to emit their ultrasonic biosonar pulses through the nostrils. This nasal emission coincides with the presence of intricately shaped baffle structures surrounding the nostrils. Some prior experimental evidence indicates that these “noseleaves” have an effect on the shape of the animals’ radiation patterns. Here, we present a numerical acoustical analysis of the noseleaf of a horseshoe bat species. We show that all three distinctive parts of its noseleaf (“lancet,” “sella,” “anterior leaf”) have an effect on the acoustic near field as well as on the directivity pattern. Furthermore, we show that furrows in one of the parts (the lancet) also exert such an influence. The underlying physical mechanisms suggested by the properties of the estimated near field are cavity resonance, as well as reflection and shadowing of the sound waves emitted by the nostrils. In their effects on the near field, the noseleaf parts showed a tendency toward spatial partitioning with the effects due to each part dominating a certain region. However, interactions between the acoustic effects of the parts were also evident, most notably, a synergism between two frequency-dependent effects (cavity resonance and shadowing) to produce an even stronger frequency selectivity.

DOI: [10.1103/PhysRevE.76.051902](https://doi.org/10.1103/PhysRevE.76.051902)

PACS number(s): 43.80.+p

## I. INTRODUCTION

Bats are a high-level grouping (an order) of mammals most noted for the use of sophisticated active and passive biosonar systems [1]. The almost 1000 species [2] of so-called “microbats” as well as some of the much less species-rich “megabats” (Old World fruit bats) emit ultrasonic biosonar pulses through their mouths or nostrils and listen to the returning echos with their ears (active sonar). Listening to signals from foreign sources (passive sonar) is also common.

Among the most conspicuous anatomical features seen in bats are the baffle shapes which surround the sites of pulse emission and echo reception. For example, the outer ears (pinnae) in the majority of bat species—while always following the general anatomical layout of a mammalian pinna—feature unusually prominent structural elements such as flaps, ridges, or grooves. The nostrils in those bat species which emit their biosonar pulses through them are surrounded by protrusions known as “noseleaves.” The two largest groups of bats with noseleaves are the New World spear-nosed bats (*Phyllostomidae*) and the Old World horseshoe bats (*Rhinolophidae*). Similar to the pinnae, bat noseleaves are rarely plain structures, but can be divided into distinct parts which are in many cases adorned with structural elements such as flaps, ridges, or furrows often not unlike their counterparts seen on the pinna.

The coincidence between the presence of noseleaves and nasal biosonar emission suggests the hypothesis that the noseleaves act as acoustic beamforming baffles which influence the shape of the emitted biosonar beam. Over the last 30 years, some preliminary experimental evidence has emerged to support this notion: It has been demonstrated that bending back the entire noseleaf changes the beam pattern in a species of spear-nosed bat [3]. Similarly, a change in beam shape was observed when the entire upper portion of a horseshoe bat’s noseleaf was covered with petroleum jelly [4].

In the work presented here, we have used numerical methods to conduct the first analysis of the acoustic function of a

noseleaf to consider all individual parts as well as one of their structural features. The goal of this work is to establish which structural features of the horseshoe bat noseleaf have acoustic effects, what these effects are, and what physical mechanisms may underlie them. In addition to the general benefits of being able to make predictions about the acoustic field in an efficient manner, the usage of numerical methods offers two important specific advantages for this work. First, the shape of the noseleaf used in the analysis is represented digitally. Therefore, it can be subjected easily to well-defined manipulations, for instance, the selective removal of individual parts without disturbing the rest of the structure. Second, the acoustic near field surrounding the noseleaf surface can be predicted along with the acoustic far-field behavior. This makes data available not only for describing the effects of structural features on the beam pattern, but also for explaining the underlying physical mechanisms.

The noseleaf studied here belongs to a horseshoe bat (genus *Rhinolophus*). Because the biosonar pulses of horseshoe bats contain narrow-band [“constant frequency” (CF)] and frequency-modulated (FM) signal components, they are included in a group called “CF-FM bats.” The bat species in this group are considered to be model organisms in physical ecology and neuroethology [5] because of the well-studied match between sensory function and ecological niche (prey detection in clutter) and the pertinent evolutionary implications [6–8].

The noseleaves of horseshoe bats consist of three distinct parts (see Fig. 1). The nostrils are surrounded at the bottom and at the sides by a smooth horseshoe-shaped baffle, the anterior leaf. Upwards from the nostrils, near the center of the noseleaf sits the sella (saddle), a peglike forward-oriented protrusion. Behind and upwards from the sella follows the lancet, which is typically deeply furrowed horizontally. The 71 horseshoe bat species of the genus *Rhinolophus* [9] differ considerably in the size and shapes of their noseleaves. As a result, the sella and the lancet in particular are often used as distinguishing features between species by biologists.

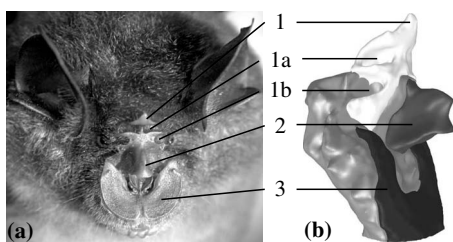


FIG. 1. The shape of the studied noseleaf and its parts. (a) Portrait photo of the individual of the Rufous horseshoe bat from which the analyzed noseleaf sample was taken. (b) Surface rendering of the noseleaf parts using a smoothed triangular mesh. The different noseleaf parts are highlighted with different gray levels: (1) lancet, (1a) upper furrow, (1b) lower furrow, (2) sella, (3) anterior leaf. The total height of the noseleaf is 11.5 mm and the furrows in the lancet are approximately 1.4 mm wide and deep.

In the work reported here, we have investigated the acoustic effects of the three parts of the noseleaf as well as the effect of the furrows in the lancet. The results on the former are reported here and the results on the latter have been published in short form already [10] but will be put into context here.

## II. METHODS

### A. Simplifying assumptions

Simplifications were made to make the acoustic problem to be analyzed more readily tractable. The shape of the noseleaf was studied in isolation from the head to keep the size of the problem small. This means that contributions by diffraction from other areas of the bat's face were not considered. No major effect on the results is expected from this simplification because of the relative location and geometry of the face as well as the size of the noseleaf (see Fig. 1). Since the bat's face is located behind a comparatively large noseleaf with facial surfaces oriented to the side and away from the noseleaf, it is expected that the noseleaf will shield the face and the weak diffracted waves from the face are even less likely to strongly interact with the forward diffraction from the noseleaf proper. Data obtained in humans [11] suggest that the influence of the head on the directivity of hearing is limited to below approximately 4 kHz. The lowest frequency used by the studied bat is about 15 times higher than this frequency. Since at the same time the noseleaf is only six to seven times smaller than a human pinna, such an influence is unlikely to be a factor that needs to be considered for the exploratory work reported here.

The surface of the noseleaf is modeled as perfectly reflecting. This is justified by the large difference in the characteristic acoustic impedance between air and tissue (four orders of magnitude). Factors such as the finite thickness and finite extent as well as the curvature of the noseleaf are unlikely to make a major difference in this situation. Experimental work comparing simulated and measured reception directivities of a bat head by different authors has confirmed that knowledge of the exact impedances is not required to obtain a numerical estimate of a directivity pattern that con-

tains the salient features and falls within the individual variability between measured specimens [12].

### B. Computer tomographic shape acquisition

A digital representation of the shape of a noseleaf sample from a Rufous horseshoe bat (*Rhinolophus rouxi*, collected in Hubei Province, China, see Fig. 1) was obtained by means of high-resolution x-ray computer tomography (Skyscan 1072  $\mu$ CT). X-ray images of the noseleaf sample were collected from directions spanning at total of  $180^\circ$  in steps of  $0.9^\circ$ . From these x-ray images, a stack of tomographic cross sections was derived by a three-dimensional cone beam reconstruction method. In the cross-section images, x-ray absorption was encoded with 256 gray levels assigned to isotropic voxels with  $30 \mu\text{m}$  edge length. The gray values in the stack of cross section were prefiltered using an isotropic Gaussian smoothing kernel and then thresholded to classify pixels as representing either air or noseleaf tissue. The resulting binary voxel representation of the noseleaf was then directly down sampled and transcribed into a finite-element mesh with linear cubic elements of  $120 \mu\text{m}$  edge length.

### C. Shape manipulation

The voxels of the digital shape representation were manually classified as belonging to either the anterior leaf, the sella, the lancet, or supporting tissue located behind and—to a lesser extent—between these parts (see Fig. 1). To study their acoustic effects, all three parts under study (anterior leaf, sella, lancet) were digitally removed from the noseleaf representation either individually or in combination to study interactions between the parts. In this way, a complete set of all possible combinations of the presence or absence of each of the three parts was created. This set contains a total of eight shapes, the original shape plus seven shapes in which either one, two, or all three parts have been removed. To create this entire set, the borders of each part of the shape had to be defined only once, all the different combinations were then created using suitable Boolean operators on the binary voxel values representing tissue and air. In the following, each shape is marked by a three-character string in which each character represents a part. “L” stands for the lancet, “S” for the sella, and “A” for the anterior leaf. A crossed-out character signifies removal of the part. For example, “L&A” denotes a shape in which the lancet and anterior leaf are present and the sella has been removed. To answer the questions whether the furrows of the lancet had an acoustic impact, the air volumes inside the furrows were filled completely with hand-placed voxels representing noseleaf tissue.

### D. Finite-element model and forward projection

The goal of the numerical simulation was to produce estimates of the acoustic near-field as well as of the far-field directivity. To derive both of these estimates in an efficient manner, a combination of a finite-element formulation for the near field and a forward projection representing undisturbed sound propagation into the far field was chosen. If only an

estimate of the directivity had been desired, a boundary-element approach [13] could have been considered as an alternative, but this method would not have yielded spatially dense estimates of near-field amplitudes in an efficient way.

The finite-element formulation was devised to find a numerical solution to the Helmholtz differential equation

$$\nabla^2\Phi + k^2\Phi = -b, \quad (1)$$

where  $\Phi$  is the sound pressure,  $k = \frac{2\pi f}{c}$  the wavenumber, and  $b$  the force term representing sources. The force term was set up to represent two point sources positioned in the nostrils and operated as a bipole, i.e., with equal magnitude and phase. Boundary conditions on the surface of the noseleaf represented perfect reflection.

Based on the geometry of the finite-element mesh representing the air volume, the entries in the element stiffness matrices  $K_{ij}^{\text{el}}$  were determined by analytically evaluating the expression

$$K_{ij}^{\text{el}} = \Delta K_{ij}^{\text{el}} - k^2 \Delta M_{ij}^{\text{el}} = \int_{V^{\text{el}}} \nabla N_i^T \nabla N_j - k^2 N_i N_j dV, \quad (2)$$

where the  $\Delta K_{ij}^{\text{el}}$  are the entries of the element acoustic stiffness matrix,  $\Delta M_{ij}^{\text{el}}$  the entries of the element acoustic mass matrix,  $N_i$  the  $i$ th shape function, and  $V^{\text{el}}$  the volume of the element. All  $K_{ij}^{\text{el}}$  are real numbers. Acoustic stiffness and mass matrices are independent of frequency and the element stiffness matrix is the same for all elements in the regular cubic finite-element mesh.

Linear shape functions were attached to the cubic finite-elements. For example, the shape function for the node  $(-1, -1, -1)$  is given in normalized local element coordinates  $(\xi, \eta, \zeta)$  by

$$N_1(\xi, \eta, \zeta) = \frac{1}{8} \times (1 - \xi) \times (1 - \eta) \times (1 - \zeta). \quad (3)$$

The shape functions for the other nodes are found by changing the sign of the local coordinates to ensure that the shape function has a value of one at its respective node and zero at all others.

On the boundary of the finite-element computational volume, reflection-free sound propagation was modeled by a layer of three-dimensional mapped wave-envelope infinite elements [14]. The entries in the element stiffness matrix of the infinite elements are given by

$$K_{ij}^{\text{el}} = \Delta K_{ij}^{\text{el}} - k^2 \Delta M_{ij}^{\text{el}} + jk \Delta C_{ij}^{\text{el}}, \quad (4)$$

where  $j$  is the imaginary unit and  $\Delta C_{ij}^{\text{el}}$  the damping term. In radial direction, Jacobi polynomials of order three with parameters  $\alpha=2$  and  $\beta=0$  were used as a basis function following a suggestion by the authors of Ref. [15]. The shape functions for the infinite elements were integrated numerically using Gauss-Legendre quadrature.

The linear problem defined by the stiffness matrix and the force vector containing the source information was solved iteratively for the complex wave-field amplitudes at the element nodes using a biconjugate gradient stabilized method [16,17] with a successive over-relaxation (SOR) preconditioner. The preconditioner's splitting matrix  $\mathbf{Q}$  is given by

$$\mathbf{Q} = \frac{1}{\omega} \mathbf{D} - \mathbf{C}_l, \quad (5)$$

where  $\mathbf{D}$  is the diagonal matrix of the system matrix (master stiffness matrix),  $\mathbf{C}_l$  its strictly lower triangular portion, and  $0 < \omega < 2$  the relaxation factor (set to a value of 1.2). The implementation of the linear system solving routines was taken from the Portable, Extensible Toolkit for Scientific Computation (PETSC) software library [18].

The relative phase of the solution to the Helmholtz equation at different points in space contains information on propagation delays which are incurred by the corresponding time-domain solution as it propagates away from the sound source. The following definition applies to the phase of the computed solutions: With longer propagation delays in the time domain, the phase values of the frequency-domain solution advance clockwise, i.e., from  $0^\circ$  to  $-90^\circ$ ,  $\pm 180^\circ$ , and  $90^\circ$ . In the description of the results, the term ‘‘phase advance’’ is used to refer to an advance in the cycle of the solution phase as occurs as a result of wave propagation away from the source. Because of these definitions, such a phase advance manifest itself in a smaller phase value, unless it crosses the boundary between phase values of  $-180^\circ$  and  $+180^\circ$ . Likewise, ‘‘phase delay’’ means that the complex phasor of the frequency-domain solution has advanced less along its cycle over a given distance from the source and will hence retain a greater value of the phase (unless the  $\pm 180^\circ$  boundary was crossed).

Based on the complex field values on surface of the finite-element computational volume, the wave was numerically projected out into the far-field projection using the Kirchhoff integral formulation [19,20]

$$\Phi(\vec{\mathbf{x}}) = -\frac{1}{4\pi} \int_S \frac{e^{jkR}}{R} \vec{\mathbf{n}} \left[ \nabla \Phi + jk \left( 1 + \frac{j}{kR} \right) \frac{\vec{\mathbf{R}}}{R} \Phi \right] ds, \quad (6)$$

where  $\vec{\mathbf{R}}$  is the vector between the surface element  $ds$  and the position  $\vec{\mathbf{x}}$ ,  $\vec{\mathbf{n}}$  the outward-pointing surface normal,  $\Phi$  the field value on  $S$ , and  $k$  the wavenumber. The product  $\vec{\mathbf{n}} \cdot \nabla \Phi = \frac{\partial \Phi}{\partial n}$  is the derivative of the field  $\Phi$  with respect to the surface normal  $\vec{\mathbf{n}}$ . This derivative was evaluated numerically by means of a three-point difference spanning the outer three layers of the finite-element mesh. To arrive at a directivity estimate, the outward projections were made to a set of points on the surface of a sphere. These points were spaced  $1^\circ$  apart in azimuth ( $\theta$ ) and elevation ( $\phi$ ), resulting in 65 160 points in total. The magnitude of the projected field values was normalized (divided by its maximum value) over all directions ( $\theta, \phi$ ) for each frequency  $f$  to produce the real-valued, normalized directivity  $0 \leq D(\theta, \phi, f) \leq 1$ .

As the Rufous horseshoe bat belongs to the group of CF-FM bats, its biosonar pulses consists of a central narrow-band portion flanked by rising and falling frequency-modulated portions at the beginning and end of the pulse, respectively (see Fig. 2). The biosonar pulses recorded from the individual studied here in a flight room ranged from 60.4 (lower edge of the FM component) to 81.5 kHz (CF component). The biosonar calls of this species have been studied extensively in the field in Sri Lanka [21]. The recordings

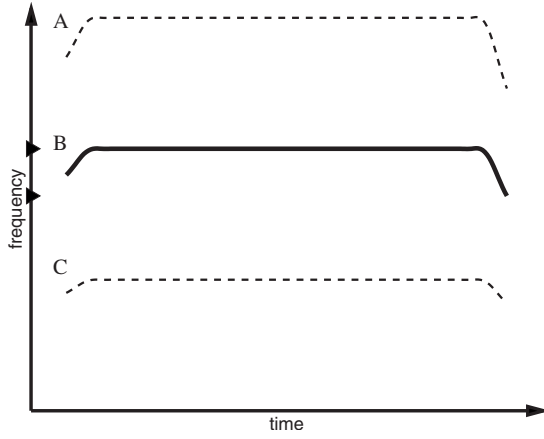


FIG. 2. Sketch of the CF-FM biosonar pulses of the Rufous horseshoe bat. The triangular markers on the ordinate mark the frequency band studied here which includes the second (strongest) harmonic [(b), solid line]. The weaker first (c) and third (a) harmonic are also shown (dashed lines, not studied here). Spectrograms of actual biosonar pulses from this species can be found in the literature [21].

obtained from the individual studied here were found to be consistent with the frequency band reported for the second harmonic (CF component between 73.5 and 79 kHz with a dependence on gender, FM bandwidth up to 16 kHz) [21]. Because the second harmonic is known to contain the most energy of all harmonics [21] and was also the only harmonic detected in the studied individual, the analysis presented here was mostly limited to the frequency band from 60 to 80 kHz. This entire band was covered by computing wave-field solutions for frequencies uniformly spaced 500 Hz apart. Given the finite-element mesh's spatial resolution of 120  $\mu\text{m}$ , the acoustic near fields for these frequencies were sampled with a resolution of 36 to 48 finite elements per wavelength. Later, the range of computations was extended downwards to 24.5 kHz and upwards to 83 kHz to gain more insight into the physical mechanisms and provide for a safety margin to account for the unknown variability in the calls of the studied individual. Over this frequency band the spatial resolution of the finite-element mesh corresponded to approximately 34 to 117 finite elements per wavelength. The frequency values were converted into wavenumbers assuming a sound speed of 343 m/s corresponding to, for example, air with a temperature of 20  $^{\circ}\text{C}$ , an adiabatic constant ( $\gamma$ ) of 1.4, and a molecular weight of 0.02895 kg/mol.

### E. Presentation of the results

If the frequency is fixed at a certain value, the resulting directivity function is a function of two angles, azimuth and elevation. It can hence be easily visualized using standard cartographic projection techniques. Here, an overview of the directivity patterns was obtained using the orthographic map projection given by [22]

$$\begin{aligned} x &= \cos \phi \sin(\theta - \theta_c), & y &= \cos \phi_c \sin \phi \\ & & & - \sin \phi_c \cos \phi \cos(\theta - \theta_c), \end{aligned} \quad (7)$$

where  $\theta_c$  and  $\phi_c$  are the azimuth and elevation of the projection center.

Three-dimensional isosurfaces of the far-field wave amplitudes were rendered to visualize the radiation beam pattern for a given frequency. In spherical coordinates, the far-field sound pressure magnitude separates into a product of two terms, the directivity and the inverse of the radius ( $r$ ) [23]:

$$|\Phi(\theta, \phi, f)| = D(\theta, \phi, f) \times \frac{1}{r}. \quad (8)$$

Hence, the radius from the source to a given isosurface  $|\Phi(\theta, \phi, f)| = C$  of the far-field magnitude is proportional to the respective value of the directivity. Plots of such isosurfaces can thus be used to conveniently visualize the shape of the three-dimensional beam pattern, which is independent of the choice of the threshold field value. The latter only affects the scale of the beam pattern which is inversely proportional to the threshold [see Eq. (8)]. Since only the shape of the beam pattern is considered here, both the chosen threshold value and the scale of the resulting graphs are not specified.

The magnitude and phase of the near-field waves have been visualized with cutting plans. On the surface of the cutting plan, the value of the quantity of interest is coded by a gray level. It should be noted that no attempt was made to unwrap the phase of the wave field, since the computational volume surrounding the noseleaf was too small to give rise to ambiguities as to the magnitude of phase changes. The phase wrapping does lead to a pattern of prominent gray-level discontinuities, however, which—while prominent features—should not be confused with actual physical discontinuities in the phase.

To assess the impact of a noseleaf part on the near field, differences in the magnitude and phase of the respective wave fields were visualized. In both cases, the simple field present when all three noseleaf parts are removed was chosen a reference. To show how the fields are changed by the manipulation, the differences in magnitude and angle of the complex field values, i.e.,  $|\Phi_1(\theta, \phi, f)| - |\Phi_2(\theta, \phi, f)|$  and  $\angle \Phi_1(\theta, \phi, f) - \angle \Phi_2(\theta, \phi, f)$  are shown. These values are in general not the same as the magnitude and phase of the difference field  $[\Phi_1(\theta, \phi, f) - \Phi_2(\theta, \phi, f)]$ . The similarity of the shape of the directivity patterns produced by the different shapes was assessed by means of a normalized correlation coefficient  $\rho_{1,2}(f)$  in spherical coordinates (with zero elevation at the equator) given by

$$\rho_{1,2}(f) = \frac{\int_{-\pi}^{+\pi} \int_{-\pi/2}^{+\pi/2} \bar{D}_1(\theta, \phi, f) \bar{D}_2(\theta, \phi, f) \cos \phi d\theta d\phi}{\sigma_1(f) \sigma_2(f)}, \quad (9)$$

where  $\bar{D}_1(\theta, \phi, f)$ ,  $\bar{D}_2(\theta, \phi, f)$  are the directivities with their mean values subtracted

$$\bar{D}(\theta, \phi, f) = D(\theta, \phi, f) - \frac{1}{4\pi} \int_{-\pi}^{+\pi} \int_{-\pi/2}^{+\pi/2} D(\theta, \phi, f) \cos \phi d\theta d\phi \quad (10)$$

and the  $\sigma_{1,2}(f)$  are given by

$$\sigma_{1,2}(f) = \sqrt{\int_{-\pi}^{+\pi} \int_{-\pi/2}^{+\pi/2} \bar{D}_{1,2}(\theta, \phi, f)^2 \cos \phi d\theta d\phi}. \quad (11)$$

**F. Error analysis**

The finite-element analysis conducted here is susceptible to numerical errors from several sources. The discretization of the domain of the solution to the Helmholtz equation and its approximation with (linear) basis functions introduce sampling and fitting errors. For well-behaved boundaries, both of these errors should decrease monotonically with the number of elements per wavelength. Since only the solution at the nodes of the finite elements is used here, the fitting error can be expected to decrease faster than  $\frac{1}{n}$ , where  $n$  is the number of elements per wavelength because of superconvergence [24]. An additional error source is the approximation of a reflection-free outward propagation by the infinite elements, which can only be approximate for a computational domain with a finite surface [25]. Finally, for the large wavenumbers associated with ultrasonic frequencies, numerical pollution effects may degrade the results [26].

In order to gauge these errors, the solution for a simplified scenario which also has an analytic solution was computed. This scenario consisted of a bipole source configuration (two equal monopole sources operating in phase) identical to the sources used in the analysis of the noseleaf but under free-field conditions (i.e., in the absence of the noseleaf). Since representation of the noseleaf surface is also a wavelength-related sampling issue, the test case is suitable to provide insights into all sources of error. However, it should be pointed out that the actual errors will depend on the shape of the solution so the results from the test case should be seen as a general indication of the accuracy achievable, but not as a definite bound on the error for the experimental solution.

For a bipole, the directivity pattern  $D(\alpha, k)$  is a bidirectional figure-of-eight given by [27]

$$D(\alpha, k) = \cos \left[ \frac{kd}{2} \cos \alpha \right], \quad (12)$$

where the angle  $\alpha$  is spanned by the direction of interest and the axis through the two point sources and  $d$  is the distance between the sources. In three dimensions, the pattern is a body-of-revolution around the axis through the two point sources. This directivity pattern has the features that can be expected in the bat, i.e., lobes and notches separating them.

The test case was numerically analyzed for three frequencies near the bottom (60 kHz), center (70 kHz), and top (80 kHz) of the band occupied by the second harmonic of the Rufous horseshoe bat. For each of the frequencies, the whole range of spatial resolutions (36 to 48 elements per wavelength) used in the study of the noseleaf were tested. From the results and the numerical evaluation of the analytical solution, the root-mean-square error as well the maximum error were computed (see Fig. 3). For the conditions used in the evaluation of the noseleaf, the root-mean-square error fell between  $\sim 1.2$  and  $\sim 1.4\%$  of the maximum value, with the maximum error between  $\sim 2.4$  and  $\sim 3.2\%$ . Over the spatial

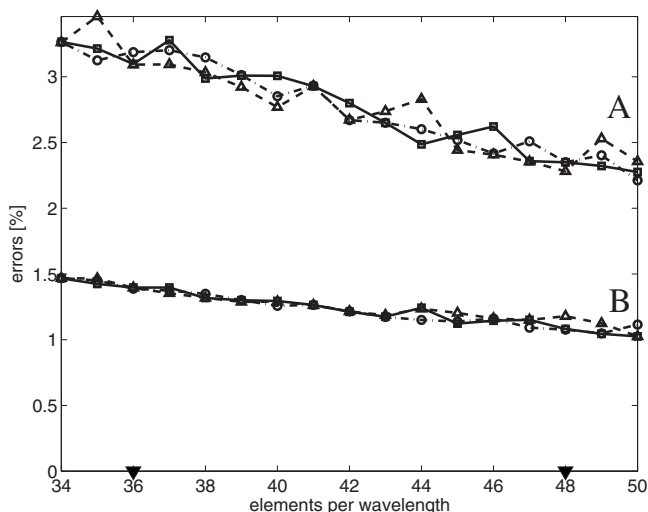


FIG. 3. Relative error in the numerical prediction of the directivity pattern of a bipole source as a function of the number of finite elements per wavelength. The upper (a) and lower (b) groups of lines marks the maximum and root-mean-square errors relative to the maximum value of the directivity gain (unity), respectively. In both groups, three lines are drawn: for the lowest (60 kHz, circles), central (70 kHz, squares), and highest frequency (80 kHz, triangles) used in the error analysis. The triangles on the abscissa mark the lowest (36) and highest (48) number of elements per wavelength used to analyze the frequency band (60 to 80 kHz) of the bats' second (strongest) harmonic.

sampling resolutions used in the analysis of the noseleaf, convergence toward the analytic solution was evident, but the difference in error between the highest and lowest resolution used amounted only to about 0.2% for the root-mean-square error and about 0.8% for the maximum error. This slow convergence of the error is expected for a sampling regime, where the error is already small. Since the error results for all three frequencies were closely aligned, there was no evidence that numerical pollution [26] was making the results obtained near the higher edge of the studied frequency band noticeably less reliable than those at the lower edge.

**III. RESULTS**

**A. Far-field directivity pattern**

The numerical predictions of beam patterns for the original ear shape showed a beam that is wider in elevation than in azimuth for all frequencies. In particular, at the higher frequencies studied, the beam patterns contained a—not fully separated—side lobe oriented downwards (see Fig. 4). This finding is in qualitative agreement with the experimental findings reported for a different species of horseshoe bat, where a prominent ventral side lobe was observed at the constant-frequency component of the biosonar pulse [4].

All studied noseleaf parts as well as the furrows in the lancet were found to have a significant impact on the shape of the radiation beam pattern, at least over part of the studied frequency band (see Fig. 4). Comparing the directivities of

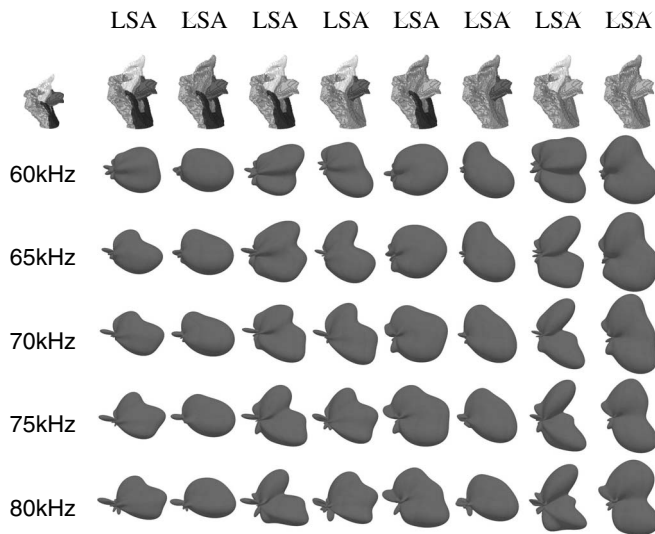


FIG. 4. Comparison of radiation beam pattern estimates for the eight different combinations of the presence and absence of the noseleaf parts lancet, sella, and anterior leaf. The shape rendering in the top left corner shows the viewing direction for all rendered beams. The three-dimensional beams shown are wave amplitude isosurfaces [28] obtained by combining the estimated directivity patterns with spherical spreading losses [see Eq. (8)]. No scale is shown since the isosurfaces scale inversely with the set amplitude threshold. The three-character code and the highlighting denote the presence or absence of the noseleaf parts. In the character string, the letters “L,” “S,” and “A” stand for the lancet, sella, and anterior leaf, respectively. Removal of a part is denoted by a crossed-out character.

the modified noseleaf shapes to the directivities of the original shape by virtue of the normalized correlation coefficient between the two functions [see Eq. (9)] yielded the following ranking of the impact of the single-part removals (see Fig. 5). Removal of the sella was found to have the biggest effect for all but the lowest frequency studied (60 kHz), where removal of the anterior leaf resulted in a slightly larger change. Removal of the lancet had the smallest effect for any single part at each frequency.

Qualitatively, the effect of removing the lancet was different from that of sella and the anterior leaf (see Fig. 4): Whereas removal of the lancet resulted in a narrower main lobe at low frequencies and the reduction of side lobes, removal of both the sella and the anterior leaf tended to cause a splitting of the main lobe into two strong lobes as well as the formation of side lobes separated from the main lobe by shallow notches.

The effects of the removal of lancet and anterior leaf showed a similar weak dependence on frequency with removal resulting in more dissimilar directivities at the low and high end of the frequency band studied (shapes  $\bar{L}SA$  and  $LS\bar{A}$  in Fig. 5). In contrast to this, the effect of sella removal depended strongly on frequency with dissimilarity increasing monotonically with frequency (shape  $L\bar{S}A$  in Fig. 5).

Filling the furrows of the lancet had a similar effect on the directivity as removing the entire lancet, the width of the beam increased significantly for the lowest frequencies stud-

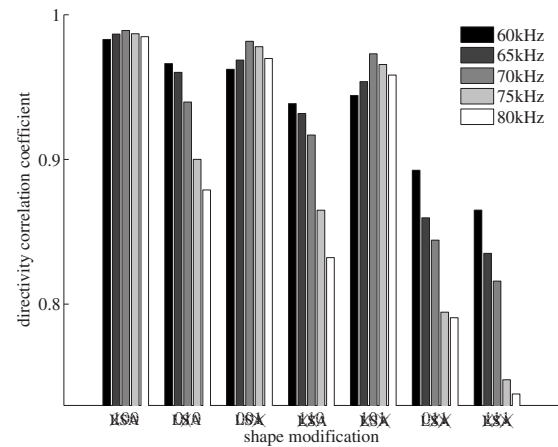


FIG. 5. Similarity between the directivity patterns of the original noseleaf and the seven shapes modified by the removal of different combinations of lancet, sella, and anterior leaf. Similarity is measured by correlation coefficients [ $\rho$ , see Eq. (9)]. The character code for the presence and or absence of the noseleaf parts is the same as in Fig. 4.

ied, in particular, in the vertical dimension (elevation). Removal of more than a single part produced evidence for interactions: For example, if the lancet was removed along with the sella, its effect on the directivity pattern was much stronger than when it was removed alone (see shapes  $\bar{L}\bar{S}A$  and  $\bar{L}S\bar{A}$  in Figs. 4 and 5). Removing the lancet along with the sella resulted in less splitting of the main beam and side lobe formation than was present when only the sella was removed. Instead, the beam widened more uniformly (see Figs. 4 and 6). A similar interaction existed between lancet and anterior leaf, although the effect of the additional lancet removal was not quite as strong. Not only were the effects of individual removal of sella and anterior leaf qualitatively similar (splitting of the main lobe), the effects also amplified each other when both parts were removed together (see Fig. 4).

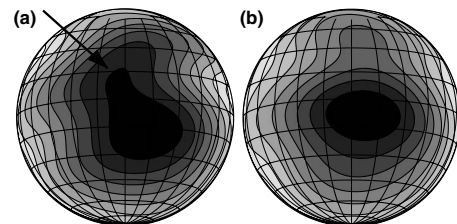


FIG. 6. Effect of filling the lancet furrows on the directivity at 60 kHz. (a) Directivity pattern for the original shape (LSA); the arrow indicates the location of the upward expansion of the beam. (b) Directivity pattern for shape with all parts of the original shape present but lancet furrows filled. The amplitude of the directivity function is linearly encoded by the gray scale, where black represents the maximum value. Contour lines are spaced 10% of the range apart. The contour estimates are based on 65 160 function values (resolution of 1° in azimuth and elevation) each. The mapping uses the orthographic projection given in Eq. (7) with  $\theta_c=0^\circ$  and  $\phi_c=-10^\circ$ . The grid lines for azimuth and elevation are both spaced 15° apart.

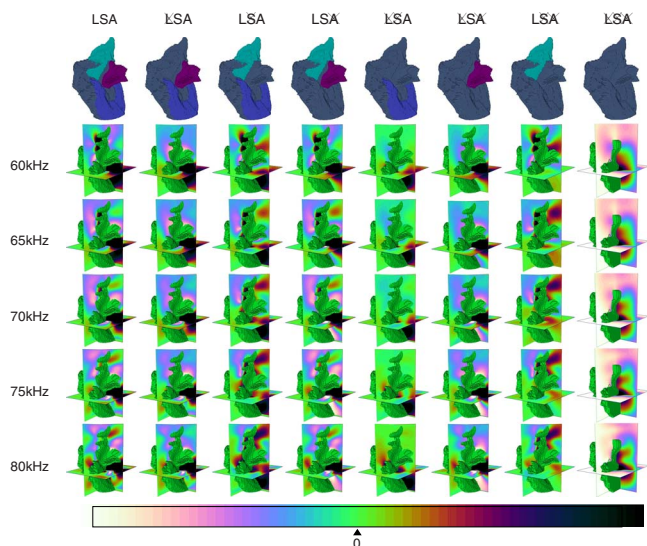


FIG. 7. (Color online) Comparison of the numerical estimates for the near-field sound pressure magnitude obtained for each of the eight different combinations of lancet, sella, and anterior leaf. The results for the shape with all parts removed (shape  $\text{L}\text{S}\text{A}$ ) are used as a reference. For this reference, the magnitudes themselves are shown, for all other shapes, the difference between the field magnitudes for the shape and the reference are shown. The coding of the absence and presence of the parts in the character string are as described for Fig. 4. Sound pressure magnitude (shape  $\text{L}\text{S}\text{A}$ ) and magnitude differences (all other shapes) on the cutting planes are encoded linearly by the color scale [29]. Since differences can be very large in some places, the range used for color encoding the differences was truncated symmetrically.

**B. Near-field magnitude**

When all three parts were removed from the noseleaf shape, the near-field amplitude in the frontal half field overall resembled the field of a bipole and only appeared disturbed to some extent in the vicinity of the remaining support tissue of the lancet. Adding the lancet alone to the support tissue (shape  $\text{L}\text{S}\text{A}$  in Fig. 7), resulted in a significant increase in the field magnitude inside the lancet furrows. This increase peaked around 60 kHz and decreased monotonically above and below this frequency (see Figs. 7 and 8). The maximum in the amplitude coincided well with the maximum difference seen between the directivities obtained for the noseleaf shapes with lancet furrows open and filled (see Figure 8).

When adding the sella alone (shape  $\text{L}\text{S}\text{A}$  in Fig. 7), the amplitude increased in a volume right below the sella and decreased in a volume above it. The latter effect became more pronounced with increasing frequency resulting in stronger decreases in the field magnitude taking place over a larger volume. In contrast to this, the volume with increases in magnitude below the sella contracted slightly with increasing frequency.

The effect of adding the anterior leaf alone (shape  $\text{L}\text{S}\text{A}$  in Fig. 7) was found to be qualitatively similar to that of the sella in that raised field magnitudes in a volume right next to the surface of the part were observed. In the case of the anterior leaf, this area bordered the bottom portion of the anterior leaf's concave surface.

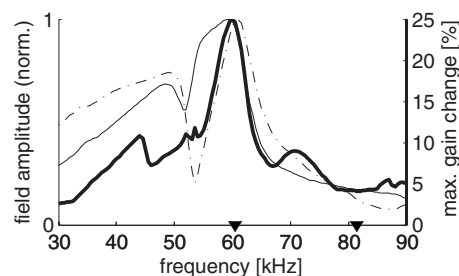


FIG. 8. Normalized sound pressure magnitudes in the lower (dashed line) and upper (thin solid line) right lancet furrow as a function of the frequency. The frequency band displayed extends beyond the range known to be used by the bat's strongest harmonic and covered by the other results presented here (marked by downward triangles) in order to show the resonance behavior unequivocally. The spacing of the data point is 500 Hz and the resonance amplitude value at each frequency was estimated based on 20 (lower furrow) or 19 (upper furrow) sample nodes located within a sphere of 0.2 mm radius, the maximum normalized standard deviation for these samples was 0.03. Superimposed on the resonance curves is the maximum change in the directivity function relative to its global maximum in percent (thick solid line).

When adding combinations of the different parts to the support tissue, interactions were again evident as they had been in the directivities: When lancet and sella were present together (shape  $\text{L}\text{S}\text{A}$  in Fig. 7), the field magnitude in the lancet furrows was reduced compared to the values obtained in these places without the sella. For the lower furrows, this decrease was also found to be frequency selective (see Fig. 9): Whereas the reduction for the lowest studied frequency (60 kHz) was about the same for the lower and upper furrow, the strength of the effect in the lower furrow increased with frequency to almost extinguish the local amplitude maximum at 80 kHz. Little interaction was obvious when lancet and anterior leaf were present together (shape  $\text{L}\text{S}\text{A}$  in Fig. 7). The changes in the vicinity of each part resembled those brought forth by the presence of that part alone.

The effect of sella and anterior leaf present together (shape  $\text{L}\text{S}\text{A}$  in Fig. 7) resembled a simple superposition of the effects the two parts had in isolation for the lowest frequencies studied (60 and 65 kHz). This superposition led to raised field magnitudes in the entire region between sella and anterior leaf. For the higher frequencies, the sella dominated the changes in the field magnitude generating a pattern which very much resembled the result obtained when only the sella was added.

The field magnitude obtained for the original shape with all three parts in place (shape  $\text{L}\text{S}\text{A}$  in Fig. 7) resembled a combination of the patterns obtained for the addition of sella and anterior leaf in the lower portion of the field (approximately from the upper edge of the sella downwards). In the upper portion of the field, the changes in magnitude were a combination of the effects of sella and lancet. Therefore, it appears that the influences of the anterior leaf and the lancet are spatially divided and limited to the lower and upper portion respectively whereas the sella exerts a significant influence on the field magnitude in the entire frontal near field.

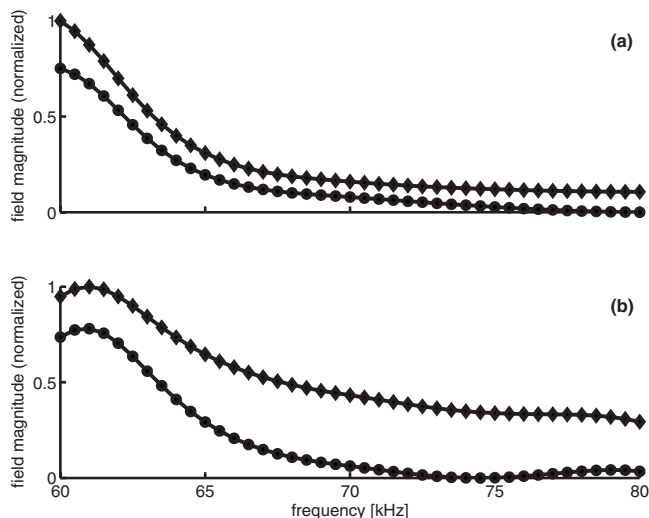


FIG. 9. Effect of the sella on the near-field magnitude in the lancet furrows. Both graphs show a normalized change in the magnitude inside a furrow between either the original shape (shape LSA, circle markers) with all three parts present or a modified shape with only the sella removed (shape LSA, diamond markers) and the shape with all three parts removed (shape LSA) as a reference. (a) Normalized near-field magnitude change in the upper furrow, (b) normalized near-field magnitude change in the lower furrow.

C. Near-field phase

As for the field magnitude, the field present when all three parts were removed from the shape was taken as a reference to judge the impact of the noseleaf parts on the near-field phase against. Again, the pattern obtained in this case was simple and indicative of spherical wave propagation with only minor disturbances by the remaining support tissue (see shape LSA in Fig. 10).

Adding the lancet alone (shape LSA in Fig. 10) causes a pattern of both phase advances and delays (compared to the situation when all parts were absent) in the area in front and to the side of the lancet. These changes were particularly large around the noseleaf furrows to the side of the lancet. The details of the pattern varied considerably with frequency, but there were some invariants in the spatial sequence of the areas with phase advances and delays.

Similar to adding the lancet, adding the sella only (shape LSA in Fig. 10) caused substantial advances and delays in the wave-field phase: Advances occurred above the sella and directly in front of the nostrils. Delays were seen to the side and immediately below the sella. The latter effect was particularly strong in the region between lancet and anterior leaf.

Adding the anterior leaf alone (shape LSA in Fig. 10) had very little influence on the wave-field phase in the half-field in front of the noseleaf, but caused phase changes behind the anterior leaf. For the lower frequencies studied (60, 65, and 70 kHz), these changes were always phase advances, whereas for the highest two frequencies (75 and 80 kHz) phase delays also occurred in a spatial region located at about half the height of the anterior leaf.

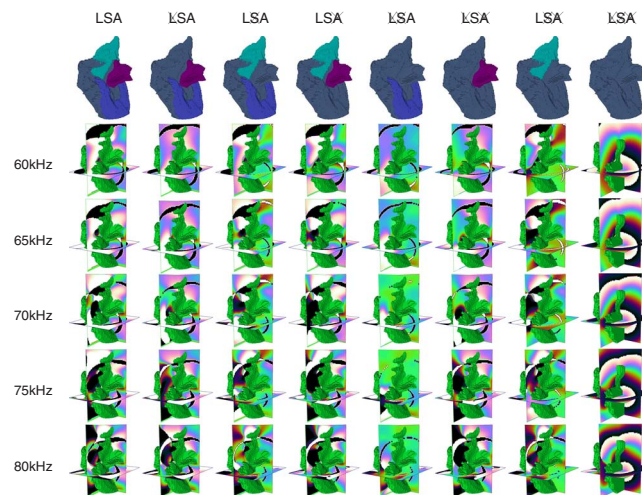


FIG. 10. (Color online) Comparison of the numerical estimates for the near-field phase obtained for each of the eight different combinations of lancet, sella, and anterior leaf. The coding of part absence and presence in the character string and the rendering are as described for Fig. 4. The shape LSA serves as a reference for which the near-field phase is shown. For all other shapes, the difference between the near-field phase of that shape and the reference is shown. The encoding of the phase and phase difference values in the color map [29] is linear and ranges from  $-180^\circ$  to  $+180^\circ$  for the phase values themselves and from  $-30^\circ$  to  $+30^\circ$  for the differences.

When adding combinations of the parts or all parts at once, the following changes were found: The effect of the joint presence of lancet and sella (shape LSA in Fig. 10) depended on the spatial location in the near field as well as on frequency: In front of the lancet and above the sella, the effect of the sella (phase advance) dominated the field even in the presence of the lancet and for all studied frequencies. To the side of the noseleaf, the situation was different: Whereas for low frequencies and in the region of the furrows the influence of lancet dominated, the phase change pattern resembled the sella effects more closely for high frequencies and well below the height of the furrows. However, the phase change patterns caused by the two parts in isolation in this region at the high frequencies were similar already.

When present together, lancet and anterior leaf (shape LSA in Fig. 10) dominated the phase change pattern in its immediate vicinity for all but the highest studied frequency, the phase pattern around each part resembled the pattern seen when the part was added by itself. Only for the highest frequency studied (80 kHz) did the phase pattern to the side of the anterior leaf resemble the one caused by the lancet more.

The spatial partitioning of the near-field phase change pattern into zones dominated by patterns which were also brought forth by one of the parts in isolation was also seen for the combination of sella and anterior leaf (shape LSA in Fig. 10). In front of the noseleaf (above as well as below the sella), the pattern resembled that caused by the sella alone for all frequencies studied. The situation to the side and behind of the noseleaf depended on frequency: For low frequencies, the phase change patterns caused by sella and an-

terior leaf alone in this region were similar and were also maintained when both parts were present together. For high frequencies the phase change pattern in this region resembled the results seen for the sella alone.

The phase change pattern induced by original shape of the noseleaf with all three parts present (shape LSA in Fig. 10) could again be explained as a patchwork where the patterns induced by the different parts in isolation were discernible in different regions: Above and below similar sella, the phase change pattern was dominated by the sella. The same was true to the side and behind the anterior leaf for high frequencies. For lower frequencies, the phase change pattern in the latter region resembled that caused by the anterior leaf alone. Around the upper portion of the noseleaf—in particular to the side near the lancet furrows—the pattern was dominated by the lancet. In summary, the situation found for the near-field phase resembled that for the near-field magnitude in that each part removed in isolation produced a spatial pattern which was still discernible in the patterns obtained for the presence of two or all parts in certain subregions of the near field.

#### IV. DISCUSSION AND CONCLUSIONS

All studied parts of the noseleaf were found to have an effect on the acoustic near field as well as on the far-field directivity pattern. The same was true for the studied part shape feature, the furrows on the lancet. These effects were strong enough to make an impact on the function of the biosonar system possible for all structures and likely at least for some of them. It has been shown in behavioral experiments that manipulating the directivity pattern of a bat's outer ear by deflecting the tragus had a significant impact on target localization for prey capture [30]. However, there is no such data available to assess the extent to which functional changes due to manipulation of the noseleaf may affect the animals sensory capabilities in higher-level tasks such as avoiding obstacles and finding food.

Thus, at minimum the relevance of these findings to the sensory biology of the animals is that none of these structural features could have been evolved as serving exclusively nonacoustic (e.g., ornamental) functions without acoustic side effects occurring at the same time. At maximum, it may be hypothesized that these shape elements have evolved into functional parts of an integrated beamforming device.

In this device, there seems to be a “division of labor” between the parts, in which the primary function of sella and anterior leaf appears to be an overall focusing of the beam, whereas the lancet in conjunction with the sella introduces a frequency-specific widening. The frequency specificity of these effects would allow the bat to use separate frequency channels for performing tasks that are better served by either wider or narrower beams on the same echo. Likely examples of biological tasks better served by wide beams could be initial scanning for prey and looking at large targets for tasks such as obstacle avoidance, landmark identification, and contour following. Examples of biological tasks for which narrower beams are likely to be advantageous could be tracking of or looking at small targets (such as insect prey) and

searching for narrow openings in large targets.

The finding that the lancet furrows are to a large extent responsible for the acoustic effect of this noseleaf part, demonstrates that structural details of the noseleaf parts should be considered as candidate features of potential acoustic relevance. This is particularly relevant, since features such as furrows, ridges, and flaps are commonplace on bat noseleaves, as well as on other facial regions, and the outer ears. It may hence be hypothesized that at least some of these features contribute significantly to the acoustic function of the structures they are part of. In addition to demonstrating the acoustic effects of the noseleaf parts and their potential functional relevance, the results presented here also provide some cues about the physical principles underlying these effects.

Among these effects, the rising magnitudes in the half-open cavities of the lancet furrows are the most readily explained. Two features in the data support the hypothesis that it is the result of a cavity resonance [10]. The two supporting this data features are the frequency and spatial specificity of the effect: As a function of frequency, the increase in the near-field magnitude shows a distinct peak surrounded by monotonically falling slopes (see Fig. 8). In space, the increase in field magnitude limited to the volume inside the furrows (see Fig. 7). For this near-field effect, a strong link to the far-field directivity could also be demonstrated as the maximum change in directivity between filled and open furrows was in agreement with the resonance frequency. Due to the resonance, the lancet furrows can act as secondary, “virtual” sound sources, so that the noseleaf has a total of six sound sources instead of only the two physical sources in the nostrils.

The effect of the sella on the near field above it and hence its interaction with the lancet can be explained as the casting of a shadow on the lancet by the sella. Although the approximations of geometrical acoustics do not apply at the ratios of sella size and wavelength (the sella is about 2.4 mm wide and 3.6 mm long from base to top; the studied wavelengths are between 4.3 and 5.7 mm) and hence there is no umbra, the diffraction around the sella can be hypothesized to cause reduced field magnitudes on the side opposite to the nostrils. Under this hypothesis, the shadow cast by the sella should get deeper as the wavelength of the sound field decreases. This was indeed evident in the data, where the maximum reduction in magnitude as well as the volume affected by it were seen to increase with frequency. The region with the deeper shadow extends up to the lower lancet furrows, but does not reach the upper furrows, which is the likely reason for the difference in the sella's effect on the two rows of furrows.

For the lower furrow, it is noteworthy that two frequency-selective effects, resonance and shadowing, reinforce each other and hence create an even stronger frequency-selective behavior (see Fig. 9). From the present findings, it cannot be decided if this reinforcement is a coincidence or the result of a coevolution of the interacting noseleaf parts. If future evidence was to support the latter hypothesis, this would have implications for the general view of the biosonar system of CF-FM bats. So far, all specific adaptations reported for the biosonar system of CF-FM bats, for example, with respect to

cochlear [31,32] and neural signal processing [5] as well as behavior [33], have been geared toward the CF portion. However, behavioral observations suggesting context-dependent allocation of signal energy to the FM portions [34] have produced indirect evidence already that the FM portions are significant to the animals, at least in certain situations. If the properties of the FM-biosonar beam described here and the noseleaf structures responsible for them were found to be adaptations, this would establish the FM portions as important components of the CF-FM biosonar system.

The results obtained here seem to indicate that both sella and anterior leaf work as shielding or reflecting baffles, which cause reflections on the side facing the source and cast shadows on the opposite side. Experimental evidence for this come from the phase advances and magnitude reductions behind these structures. The significant increases in the near-field magnitude seen right in front of the sella and anterior-leaf surfaces facing the nostrils could be interpreted as amplification in a “pressure zone” through in-phase reflection. The thickness of these zones—slightly less than half a wavelength and decreasing with increasing frequency—is in agreement with this hypothesis. Not only do the sella and anterior leaf seem to act on the near field through similar mechanisms, their effects on the far-field directivity are likewise similar, both focus the beam and their removal leads to a splitting of the beam which is enhanced if both parts are removed together (see Fig. 4).

Of all single part removals, removal of the sella had the biggest effect on the directivity (see Fig. 5). This is matched by the role the sella plays in shaping magnitude and phase of the near field: For the magnitude, the effect of the sella combines with the anterior leaf for lower frequencies and dominates it for high frequencies. The sella also exerts an influence on the lancet by shadowing it. For the phase, the sella effects dominate the other parts over most of the near field. The only exception are the volume in and immediately around the lancet furrows and the region behind the anterior leaf and in both cases the phase pattern brought forth by the other parts only prevails at low frequencies.

Together, the acoustic effects of sella and lancet stand out for their strong impact on the directivity pattern (sella overall, lancet for low frequencies), strong frequency selectivity, and interaction with each other. Horseshoe bat species are also most variable in the shapes of their sellas and lancets [9], therefore some of these interspecific differences may be candidates for adaptations of the beamforming by the noseleaf to the animals’ specific needs. An example may be the extraordinarily long sella in Bourret’s horseshoe bat (*Rhinolophus paradoxolophus* [35]).

In addition to these interspecific differences, the existence of individual variability in the noseleaf shape and its resulting acoustic properties is highly likely. Since the results presented here were obtained from a single specimen, the discussed features of the data have been limited to effects that

are qualitatively linked to the presence, approximate size, and relative location of the noseleaf parts but not to the exact individual layout. Individual noseleaf anatomies may, for example, differ in the volume and shape of the lancet furrows or the size and shape of the sella. Such differences can be expected to affect the resonance frequency of the furrows or the extent to which the sella shadows the furrows at different frequencies. However, as long as lancet, sella, and horseshoe are present in their approximate shape and placement (e.g., sella between sound source and lancet furrows), the effects discussed here are almost certain to be present. The possible modifying influence of individual variability on these properties raises interesting questions as to how other portions of the biosonar systems may be adapted to work together on an individual level. For instance, it could be that the resonance frequency of the furrows is correlated with the lower edge of the frequency band used by the bats.

Sella and lancet are also structures which set the shape of the noseleaf apart from technical beamforming baffles. Whereas shapes similar to that of the anterior leaf may be seen in passive reflectors for technical antennas [27], the function of the lancet and the sella may be looked into for principles which could be used in engineering applications. In order to do so successfully, a better deeper understanding of the mechanisms and how they relate to the specific shapes would be desirable.

The present work has been limited to demonstrating that each noseleaf part has acoustic effects and the presence of interactions between them. The data obtained suffices to demonstrate one physical effect (resonance) unequivocally, hints at another (amplification through in-phase reflection), but does not clarify all underlying mechanisms. Future work on the shapes of horseshoe noseleaves is needed to fully understand the physics behind the less well localized effects and the interactions between parts. This is difficult, since the approximations of geometric acoustics cannot be used, so other ways have to be found to make the processes comprehensible. The same is true for developing a better understanding of the mechanisms linking the near-field effects to the far-field directivity. Although all causes of the directivity pattern are to be found in the near field, the relationship between the two is not necessarily intuitive since the complex field amplitudes over an entire surface surrounding the noseleaf have to be considered. If it is possible to extract simple principles from these complicated relationships, these principles could be analyzed for their technical value and used to understand the variability in the biological noseleaf shapes better.

#### ACKNOWLEDGMENTS

This work was supported by the European Commission (CILIA project) and research funds from Shandong University.

- [1] D. Griffin, *Listening in the Dark* (Cornell University Press, Ithaca, 1986).
- [2] N. Simmons, *Mammal Species of the World: A Taxonomic and Geographic Reference*, 3rd ed. (Johns Hopkins University Press, Baltimore, 2005), Vol. 1, pp. 312–529.
- [3] D. J. Hartley and R. A. Suthers, *J. Acoust. Soc. Am.* **82**, 1892 (1987).
- [4] H.-U. Schnitzler and A. D. Grinnell, *J. Comp. Physiol. [A]* **116**, 51 (1977).
- [5] C. F. Moss and S. R. Sinha, *Curr. Opin. Neurobiol.* **13**, 751 (2003).
- [6] J. A. Simmons and R. A. Stein, *J. Comp. Physiol. [A]* **135**, 61 (1980).
- [7] H. Arita and M. Fenton, *Trends Ecol. Evol.* **12**, 53 (1997).
- [8] G. Jones and E. C. Teeling, *Trends Ecol. Evol.* **21**, 149 (2006).
- [9] C. Csorba, P. Ujhelyi, and N. Thomas, *Horseshoe Bats of the World* (Alana Books, Bishop's Castle, Shropshire, UK, 2003).
- [10] Q. Zhuang and R. Müller, *Phys. Rev. Lett.* **97**, 218701 (2006).
- [11] E. A. López-Poveda, Ph.D. thesis, Loughborough University, Leicestershire, UK (1996).
- [12] F. D. Mey, J. Reijniers, H. Peremans, M. Otani, and U. Firzlaff, *J. Acoust. Soc. Am.* (to be published).
- [13] B. F. G. Katz, *J. Acoust. Soc. Am.* **110**, 24408 (2001).
- [14] R. J. Astley and G. J. Macaulay, *J. Acoust. Soc. Am.* **103**, 49 (1998).
- [15] D. Dreyer and O. von Estorff, *Int. J. Numer. Methods Eng.* **58**, 933 (2003).
- [16] R. Barrett, M. Berry, T. F. Chan, J. Demmel, J. Donato, J. Dongarra, V. Eijkhout, R. Pozo, C. Romine, and H. V. der Vorst, *Templates for the Solution of Linear Systems: Building Blocks for Iterative Methods*, 2nd ed. (SIAM, Philadelphia, PA, 1994).
- [17] H. A. van der Vorst, *Iterative Krylov Methods for Large Linear Systems, Cambridge Monographs on Applied and Computational Mathematics* (Cambridge University Press, Cambridge, UK, 2003).
- [18] S. Balay, W. D. Gropp, L. C. McInnes, and B. F. Smith, in *Modern Software Tools in Scientific Computing*, edited by E. Arge, A. M. Bruaset, and H. P. Langtangen (Birkhäuser Press, New York, 1997), pp. 163–202.
- [19] D. E. Jackson, *Classical Electrodynamics*, 3rd ed. (John Wiley & Sons, New York, 1999).
- [20] O. M. Ramahi, *IEEE Trans. Antennas Propag.* **45**, 753 (1997).
- [21] G. Neuweiler, W. Metzner, U. Heilmann, R. Rübsamen, M. Eckrich, and H. Costa, *Behav. Ecol. Sociobiol.* **20**, 53 (1987).
- [22] E. W. Weisstein, *CRC Concise Encyclopedia of Mathematics*, 2nd ed. (CRC Press, Boca Raton, FL, 2002).
- [23] R. J. Urick, *Principles of Underwater Sound*, 3rd ed. (McGraw-Hill, New York, 1983).
- [24] O. Zienkiewicz, R. Taylor, and J. Zhu, *The Finite Element Method: Its Basis and Fundamentals*, 6th ed. (Elsevier Butterworth-Heinemann, London, 2005).
- [25] B. Engquist and A. Majda, *Math. Comput.* **31**, 629 (1977).
- [26] F. Ihlenburg, *Finite Element Analysis of Acoustic Scattering* (Springer, New York, 1998).
- [27] J. Kraus and R. Marhefka, *Antennas: For all Applications* (McGraw-Hill, New York, 2002).
- [28] See EPAPS Document No. E-PLLEE8-76-031711 for an alternative representation of the patterns using two-dimensional maps of directivity gain. For more information on EPAPS, see <http://www.aip.org/pubservs/epaps.html>.
- [29] J. McNames, *IEEE Signal Process. Mag.* **23**, 82 (2006).
- [30] C. Chiu and C. F. Moss, *J. Acoust. Soc. Am.* **121**, 2227 (2007).
- [31] V. Bruns and E. Schmieszek, *Hear. Res.* **3**, 27 (1980).
- [32] M. Kössl, *Hear. Res.* **72**, 59 (1994).
- [33] H.-U. Schnitzler, *J. Comp. Physiol. [A]* **82**, 79 (1973).
- [34] B. Tian and H.-U. Schnitzler, *J. Acoust. Soc. Am.* **101**, 2347 (1997).
- [35] J. L. Eger and M. B. Fenton, *Mamm. Species* **731**, 1 (2003).